AGU PUBLICATIONS

Geochemistry, Geophysics, Geosystems

RESEARCH ARTICLE
10.1002/2017GC007127

Special Section:
Magnetism From Atomic to Planetary Scales: Physical Principles and Interdisciplinary Applications in Geo- and Planetary Sciences

Key Points:
- Depth variation of magnetofossil morphologies in pelagic red clay around Minamitorisima, western North Pacific
- Discovery of a layer with enhancement of bullet-shaped magnetofossils
- Potential paleoenvironmental record in red clay

Correspondence to:
Y. Usui,
yoichi@jamstec.go.jp

Citation:
Usui, Y., Yamazaki, T., & Saitoh, M. (2017). Changing abundance of magnetofossil morphologies in pelagic red clay around Minamitorishima, Western North Pacific. *Geochemistry, Geophysics, Geosystems*, *18*, 4558–4572. https://doi.org/10.1002/2017GC007127

Received 11 JUL 2017
Accepted 27 NOV 2017
Accepted article online 8 DEC 2017
Published online 22 DEC 2017

Changing Abundance of Magnetofossil Morphologies in Pelagic Red Clay Around Minamitorishima, Western North Pacific

Yoichi Usui[1,2,3], Toshitsugu Yamazaki[2,3,4], and Masafumi Saitoh[2,3]

[1]Department of Deep Earth Structure and Dynamics Research, Japan Agency for Marine-Earth Science and Technology (JAMSTEC), Yokosuka, Kanagawa, Japan, [2]Research and Development Center for Submarine Resources, JAMSTEC, Yokosuka, Kanagawa, Japan, [3]Project Team for Development of New-generation Research Protocol for Submarine Resources, JAMSTEC, Yokosuka, Kanagawa, Japan, [4]Atmosphere and Ocean Research Institute (AORI), University of Tokyo, Kashiwa, Chiba, Japan

Abstract Recent investigations have discovered an unexpected abundance of magnetofossils in oxic pelagic red clays. These have potential to serve as paleoenvironmental tracers in otherwise nonfossiliferous sediments. Here, we report on variations in the abundance and morphology of magnetofossils in red clay from the western North Pacific. Magnetic measurements revealed that magnetofossils dominate the magnetic mineral assemblage of the sediments. An endmember analysis of isothermal remanent magnetization acquisition curves, supplemented by an analysis of S ratios, indicates that the magnetic assemblage can be unmixed into three endmembers, two corresponding to magnetofossils and one to terrigenous magnetic minerals. Direct counting of magnetofossil morphologies under a transmission electron microscope shows that the two magnetofossil endmembers differentiate equant magnetofossils and bullet-shaped magnetofossils, respectively. The stratigraphic variation of the endmember contributions revealed that the equant magnetofossils are dominant for the most part, while an interval at around 7 m in core depth shows higher abundance of the bullet-shaped magnetofossils. This may reflect enhanced organic carbon flux to the sediments. The organic carbon content is low throughout the sediments, and it does not show any change corresponding to the increase of bullet-shaped magnetofossils, pointing at extensive remineralization of the organic carbon. On the basis of lithostratigraphic correlation to nearby drilling sites, we tentatively estimate the age of the bullet-shaped magnetofossil increase as sometime between ~75 and 25 Ma. These results suggest that environmental information can be obtained from magnetofossils in pelagic red clay.

Plain Language Summary Ocean is important to understand global environmental change, and past marine environment is often estimated using fossils. However, abyssal sediments, which cover large part of world ocean floor, is generally non-fossiliferous. We studied magnetic mineral magnetite produced by microbes in such deep sea sediments. Those magnetites can be considered as fossils (magnetofossils), and they should also record past environment. We have discovered a layer with enhancement of bullet-shaped magnetofossils in abyssal western North Pacific. Our results demonstrate that abyssal environment may be variable in geological history, and changes can be recovered using magnetofossils.

1. Introduction

Magnetofossils are the geological remnants of magnetosomes (biomineralized ferromagnetic crystals) of magnetotactic bacteria (Kirschvink & Chang, 1984; Petersen et al., 1993; Stolz et al., 1986). Magnetotactic bacteria are found in wide variety of settings such as oligotrophic oxic sediments from the deep sea (Yamazaki & Shimono, 2013), high temperature hot springs (Lefèvre et al., 2010), or alkaline lakes (Lefèvre et al., 2011); therefore, magnetofossils may be unique biogeochemical tracers in otherwise nonfossiliferous environments. The environmental information carried by magnetofossils have been investigated by documenting their abundance and morphology (Egli, 2004a; Heslop et al., 2014; Hesse, 1994; Roberts et al., 2011; Yamazaki & Kawahata, 1998). In addition to direct microscopic observations, magnetic techniques have been used to quantify and characterize magnetofossils in bulk sediments (Egli, 2004a; Egli et al., 2010; Kopp et al., 2006; Li et al., 2012).

The controlling factors of magnetofossil abundance in oligotrophic sediments appear to be different from those in sediments with higher organic carbon flux. A conventional model proposes that enhanced magnetofossil production represents the expansion of the oxic-anoxic transition zone in sediments, which can be achieved through decreased organic carbon supply, increased oxygen supply, or increased sedimentation rate (Dinarès-Turell et al., 2003; Hesse, 1994; Kopp & Kirschvink, 2008; Kopp et al., 2007; Lean & McCave, 1998; Petermann & Bleil, 1993). In contrast, for oligotrophic pelagic carbonates, Roberts et al. (2011) documented that magnetofossil abundance correlates with organic carbon flux estimated from corresponding nannofossil assemblages. A similar pattern has been reported for other pelagic carbonates from northeastern Apennines (Savian et al., 2014). The redox zonation of these sediments are already expanded due to low organic carbon flux, and it is proposed that availability of organic carbon is the limiting factor of the metabolism of magnetotactic bacteria and subsequent magnetofossil abundance in these sediments (Roberts et al., 2011). In addition, the magnetofossil abundance and the organic carbon flux also positively correlate with Eolian dust content (Roberts et al., 2011; Savian et al., 2014). These authors argue that the deposition of liable iron minerals as Eolian dust may have enhanced surface productivity to increase the organic carbon flux to the seafloor. Furthermore, iron may have been delivered to the seafloor and directly utilized in magnetofossil production by magnetotactic bacteria. The positive correlation between magnetofossil abundance and dust deposition has been also reported for other pelagic carbonates (Yamazaki, 2012; Yamazaki & Ikehara, 2012).

Several studies have documented magnetofossil morphologies in marine settings (Hesse, 1994; Lean & McCave, 1998; Vali et al., 1989; Yamazaki, 2012; Yamazaki & Ikehara, 2012; Yamazaki & Kawahata, 1998). Stratigraphic variation of magnetofossil morphologies was investigated in deep sea hemipelagic sediments (Hesse, 1994), contourite drift (Lean & McCave, 1998), and pelagic nannofossil ooze (Yamazaki, 2012; Yamazaki & Ikehara, 2012). In the hemipelagic sediments in the Tasman Sea and the pelagic nannofossil ooze in the Southern Ocean and the Pacific, the ratio of isotropic magnetofossils to elongated magnetofossils and inferred oxygen concentration in surface pore water both decreased in glacial stages. Hesse (1994) was the first to propose that isotropic magnetofossils indicate a more oxic environment compared to elongated magnetofossils. The same conclusion was reached by Yamazaki and Kawahata (1998) by studying the geographical variation of magnetofossil morphology in western Pacific surface sediments with different organic carbon flux. Several studies used magnetic techniques to unmix different magnetofossil morphologies, and anisotropic magnetofossils have been shown to have higher coercivity than isotropic ones (Lascu & Plank, 2013; Yamazaki, 2012; Yamazaki & Ikehara, 2012). However, care should be taken because one study documented that isotropic magnetofossils increased when organic carbon flux was high in a contourite drift of the northern flank of Chatham Rise (Lean & McCave, 1998). It has also been speculated that the geomagnetic intensity may affect the size of magnetofossils (Farina et al., 1994; Lin et al., 2014). Heslop et al. (2014) analyzed marine sediment cores from various regions, and revealed that each sediment sequence exhibits a distinct trend in its magnetic characteristics, which possibly reflects mixing of multiple morphologies. It is thus essential to investigate a wide range of geological settings to fully understand the paleoenvironmental information carried by magnetofossils.

Pelagic red clay has gathered little attention in magnetofossil studies; the very low organic carbon flux and deep penetration of oxygen to the sediments (e.g., D'Hondt et al., 2015) prevents the development of the oxic-anoxic transition zone where magnetotactic bacteria often inhabit (Kopp & Kirschvink, 2008; Petermann & Bleil, 1993), and red clay provinces are considered to be monotonous and in a stable environment. The first point has been challenged by the discovery of abundant magnetofossils from red clay (Shimono & Yamazaki, 2016; Vali et al., 1989; Yamazaki & Ioka, 1997; Yamazaki & Kawahata, 1998; Yamazaki & Shimono, 2013) and some pelagic carbonate with similarly low organic carbon content without any sign of anoxic diagenesis (Petersen et al., 1993; Roberts et al., 2011, 2013). The biogeochemical variability in pelagic sediments has also been recognized. In the present oceans, tens of meters scale oxygen penetration to sediments has been detected in the South Pacific Gyre (D'Hondt et al., 2009, 2015; Fischer et al., 2009), the North Atlantic Gyre (Ziebis et al., 2012), and the central North Pacific Gyre (Røy et al., 2012). On the other hand, oxygen is exhausted within the top few meters of sediments beneath regions with relatively higher surface productivity (D'Hondt et al., 2009; Røy et al., 2012) even in brownish clayey sediments (Mewes et al., 2014). Deep penetration of oxygen fosters diverse aerobic communities (D'Hondt et al., 2015), whereas relatively shallow oxygen penetration promotes biogeochemical redox cycling of elements such as Mn and N in

the suboxic zone below (Mogollón et al., 2016). Over geological timescales, changing Eolian flux (e.g., Rea, 1994), ocean circulation (e.g., Cramer et al., 2009), and marine ecological structures (e.g., Norris et al., 2013) may have modified organic carbon flux to and oxygenation in pelagic red clay provinces, and these changes may have been recorded in magnetofossils. In this study, we report the first systematic study of magnetofossil abundance and morphology variations in pelagic red clay.

2. Sample

We study the piston core PC12 obtained during R/V Mirai cruise MR15-E01 Leg2 in the western North Pacific Ocean in March 2015 (Nozaki, 2015). The piston core was retrieved at 22°04.2191′N, 153°50.5017′E with core length of 11.234 m (Figure 1).

The site is located ~260 km south of the island Minamitorishima (also known as Marcus Island). Many seamounts are in the area, representing part of the Marcus-Wake Seamounts. Nevertheless, the seafloor between the seamounts is almost flat. The site is ~160 km east from the Ocean Drilling Program Site 800 (Lancelot et al., 1990), and ~14 km northwest from the PC05 of KR13-02 cruise (Iijima et al., 2016). No major seamounts exists between these sites (Figure 1b). The water depth at the site is 5,777 m. The core was cut into 11 sections of ~1 m length. One interstitial water sample per section was taken by Rhizon (not used in this study). The sections were then split and described on the ship (Nozaki, 2015).

The samples used in this study were collected using 7 cc plastic cubes from the section halves curated in the Kochi Institute for Core Sample Research. The cubes were taken continuously, and every fourth cube was used in this study, resulting in a measurement spacing of ~10 cm. Samples were not taken between 3.20 and 3.97 m in core depth due to core disturbance. The sediments are mainly composed of dark brown to brownish black pelagic clay (supplementary material). Sediment color becomes progressively darker downward to ~5.3 m. At ~5.3 m, a sudden change to slightly lighter color with convoluted and interfingered interfaces was observed, potentially indicating a hiatus. Between ~7.6 and ~8.6 m, the sediment exhibits color alternations of brown and yellowish brown with a 0.5–1 cm cyclicity. The color alternation gradually vanishes both upward and downward. Below the color alternation zone, sediment color is slightly lighter with irregular yellowish streaks. Shipboard smear slide observations revealed that the major components of the sediments are clay minerals, ferromanganese oxides and quartz, with a variable amount of euhedral phillipsite and biogenic apatite. A sporadic, very rare occurrence of microfossils with poor preservation leaves the age of sediments unknown.

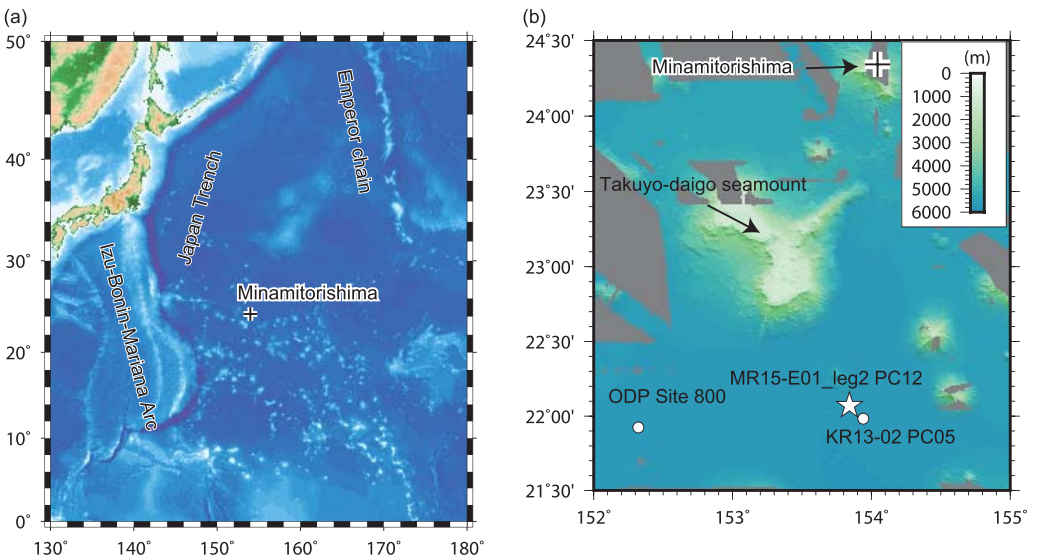

Figure 1. (a) Regional map of western North Pacific area showing the location of Minamitorishima and major bathymetric features. Bathymetric data are ETOPO1. (b) Detailed bathmetry and the location of the study site MR15-E01 leg2 PC12 (star), together with the locations of Minamitorishima (cross), KR13-02 PC05, and ODP Site 800 (circles).

3. Methods

3.1. Anhysteretic Susceptibility and First-Order Reversal Curve

Magnetofossils are characterized by a narrow coercivity distribution with minimal magnetostatic interactions due to biologically controlled sizes and arrangement of the crystals (Egli et al., 2010; Kopp & Kirschvink, 2008; Li et al., 2012), although magnetofossils can exhibit interactions if the original arrangement has collapsed (Kobayashi et al., 2006). We use the ratio of susceptibility of anhysteretic remanent magnetization (*k*ARM) to saturation isothermal remanent magnetization (SIRM) (Egli, 2004a; Li et al., 2012), and first-order reversal curve (FORC) diagrams (Egli et al., 2010; Roberts et al., 2014) to detect these features.

Anhysteretic remanent magnetization (ARM) was imparted and measured using a cryogenic magnetometer system (2G Enterprises 755R) with a peak alternating field of 80 mT and a DC bias field of 0.1 mT at JAMSTEC. SIRM was imparted using a pulse magnetizer (2G Enterprises 660) with a 2.7 T field, and measured using a spinner magnetometer (Natsuhara Giken ASPIN) at JAMSTEC.

For FORC measurements, ~1 cc of sediment was subsampled from selected 7 cc cubes, resulting in 21 samples for FORCs with the measurement frequency of ~50 cm. FORCs were measured using a vibrating sample magnetometer (VSM, Princeton Measurements model 2900) with a custom-made holder to accommodate wet 1 cc samples at JAMSTEC. The field spacing was 0.5 mT. Obtained FORCs were analyzed using VARIFORC software (ver. 3.02; Egli et al., 2010) to generate FORC diagrams (Pike et al., 1999). For all samples, we used $S0 = 8$ and $\lambda = 0.1$ for the smoothing specification parameters, and $Hb0 = 0.0004$, $sb0 = 3$, and $w0 = 0.0005$ for the vertical smoothing factor parameters (Egli et al., 2010). A complete parameter list is provided in the supporting materials.

3.2. S Ratios and IRM Acquisition Analysis

Egli (2004a) reported that both marine and lake sediments contains two groups of magnetofossils with distinct coercivity distributions. Heslop et al. (2014) confirmed the mixing of two groups of magnetofossils in marine sediments; at the same time, however, they emphasized the intrasequence variability, indicating that either of the two groups is not universal among various regions or environments. We use S ratios (Thompson & Oldfield, 1986) and isothermal remanent magnetization (IRM) acquisition analysis (Robertson & France, 1994) to distinguish magnetic components.

S ratios were calculated following the definition of Bloemendal et al. (1988). SIRM measurements were followed by IRMs imparted by lower back fields. IRMs were imparted using the pulse magnetizer and measured using the spinner magnetometer. We used three back field magnitude of 0.03, 0.1, and 0.3 T to calculate three S ratios, designated as $S_{-0.03}$, $S_{-0.1}$, and $S_{-0.3}$, respectively. $S_{-0.3}$ measures the fraction of magnetization not carried by high-coercivity antiferromagnetic minerals such as hematite and goethite. $S_{-0.1}$ measures the fraction of low coercivity mineral magnetization which typically corresponds to magnetite. Importantly, magnetization of magnetofossils mostly saturates with the 0.1 T field. In contrast, terrigenous magnetic minerals in North Pacific pelagic sediments are often of higher coercivity, because they are mainly fine-grained, distal Eolian particles (Rea, 1994). Consequently, $S_{-0.1}$ in pelagic sediments often reflects the fraction of magnetization of magnetofossils against that of terrigenous magnetic minerals (Yamazaki, 2008, 2009, 2012). $S_{-0.03}$ is not widely used, but we expect this parameter can provide clues about different magnetofossil groups, as magnetofossils typically have median coercivity of 0.02–0.07 T (Egli, 2004a; Heslop et al., 2014; Lascu & Plank, 2013; Moskowitz et al., 1993). The 21 samples used in the FORC measurements were subsampled before the measurement of $S_{-0.03}$. Out of the 21 samples, 10 samples were measured for $S_{-0.03}$ using the ~1 cc samples. The other 11 samples were dried before the measurement of $S_{-0.03}$, so their $S_{-0.03}$ were not used in the analysis.

IRM acquisition curves were measured using the VSM on the ~1 cc subsamples used in the FORC measurements; the measurements were made with 100 nonlinear field steps from 0.5 mT to 1.0 T. The IRM acquisition curves were analyzed by the endmember modeling method using IRM-Unmixer software (Heslop & Dillon, 2007). Before this analysis, we always removed the two data points at ~30 and ~100 mT field steps, because the IRM curves showed systematic and reproducible jumps at those field steps, most likely reflecting small calibration error of the VSM (we have checked that the results of the end-member modeling are not changed by this processing step). The remaining 98 IRM values were interpolated using cubic splines, and IRMs corresponding to applied fields from 5 to 300 mT were fed into the software. The volume normalized IRM magnitude at 300 mT was estimated from SIRM and $S_{-0.3}$.

3.3. Electron Microscopy

Magnetic mineral extracts of selected samples were investigated with a transmission electron microscope (TEM). To extract magnetic minerals, the sediments were first dispersed completely in distilled water with sodium hexametaphosphate using an ultrasonic bath, and then magnetic minerals were collected using a "magnetic finger" (Kirschvink et al., 1992; Petersen et al., 1993; von Dobeneck et al., 1987). The magnetic extracts were dispersed in ethanol, and a small drop of the suspension was dried on a carbon-coated copper grid. A TEM operated at 120 kV (JEOL JEM-1400) at the Atmosphere and Ocean Research Institute, the University of Tokyo, was used for the observations. From the morphology in TEM images, magnetofossils were classified into three groups: bullet-shaped, elongated, and equant. The elongated group mainly consists of hexagonal prisms and elongated octahedra. Cubo-octahedra represent the equant group, and short hexagonal prisms of length/width ratios close to one may also be included in this group. More than 1,000 grains on about 100 images were counted for each sample. The classification is semiquantitative; some ambiguity remains in judging three-dimensional morphology from an image projected on a plane. Nonetheless, the bullet-shaped crystals can easily be identified from their unique morphology.

3.4. Organic Carbon Content

After the ~1 cc subsamples were taken for the FORC measurements, we used the remaining material to measure total organic carbon (TOC) content. The samples were powdered and treated with 6 M HCl for ~24 h to dissolve all the carbonate. The residue was purified by repeated centrifugation adding ultrapure water and was then dried at 80°C for 48 h. About 50 mg of the residue was placed into a tin cup, and the TOC content was measured by a FLASH 2000 Elemental Analyzer (Thermo Scientific). The analytical reproducibility of the TOC contents determined by replicate analyses of laboratory standards is better than 0.01%.

4. Results

4.1. Anhysteretic Susceptibility and First-Order Reversal Curves

Both the *k*ARM/SIRM ratio and the FORC diagrams suggest the dominance of magnetofossils in the sediments. The *k*ARM/SIRM values ranges from 0.8 to 2.5 mm/A. These high values indicate relatively small magnetostatic interactions, and are comparable to the values reported from red clay from the South Pacific Gyre that contain abundant magnetofossils (Yamazaki & Shimono, 2013). The *k*ARM/SIRM values are ~2.5 mm/A below ~5.3 m, and decrease sharply up-core to ~0.8 mm/A (Figure 2a). This shift may coincide with a possible hiatus implied by the sharp core color change. The SIRM magnitude exhibits a broad high around 7 m (Figure 2b), and the jump in *k*ARM/SIRM does not accompany a major change in the SIRM magnitude.

The FORC diagrams revealed clear central ridges (Figures 2c–2f) indicating the dominance of noninteracting stable single domain particles. This often represents magnetofossils in sediments (Egli et al., 2010). The central ridge is more prominent below ~5.3 m; above this depth, the FORC diagrams shows some vertical spread. Together, the sediments above ~5.3 m likely contain higher proportions of terrigenous magnetic minerals.

4.2. S Ratios and IRM Acquisition Analysis

The S ratios exhibit distinct depth variations (Figures 3a–3c). $S_{-0.3}$ values are close to 1.0 in the lower part, and gradually decreases from ~5.3 m. $S_{-0.1}$ likewise decrease up-core from ~1.0 below ~5.3 m to ~0.83 at the core top. These values are very close to the values reported from the South Pacific Gyre (Shimono & Yamazaki, 2016). The up-core trend is consistent with an increased importance of terrigenous magnetic minerals above ~5.3 m that was also suggested by the *k*ARM/SIRM ratio and the FORC diagrams.

The variation of $S_{-0.03}$ is similar to that of $S_{-0.3}$ and $S_{-0.1}$ above ~5.5 m. This can be explained by the up-core increase of terrigenous magnetic minerals with coercivity distribution extending above 0.3 T. However, below ~5.5 m, $S_{-0.03}$ behaves differently from the other S ratios; while $S_{-0.3}$ and $S_{-0.1}$ stay at near constant high values, $S_{-0.03}$ features a pronounced decrease from 11 to 7 m followed by a sharp increase up to 5.5 m. We examine the relationship between $S_{-0.1}$ and $S_{-0.03}$ in a cross plot (Figure 3d) which shows the presence

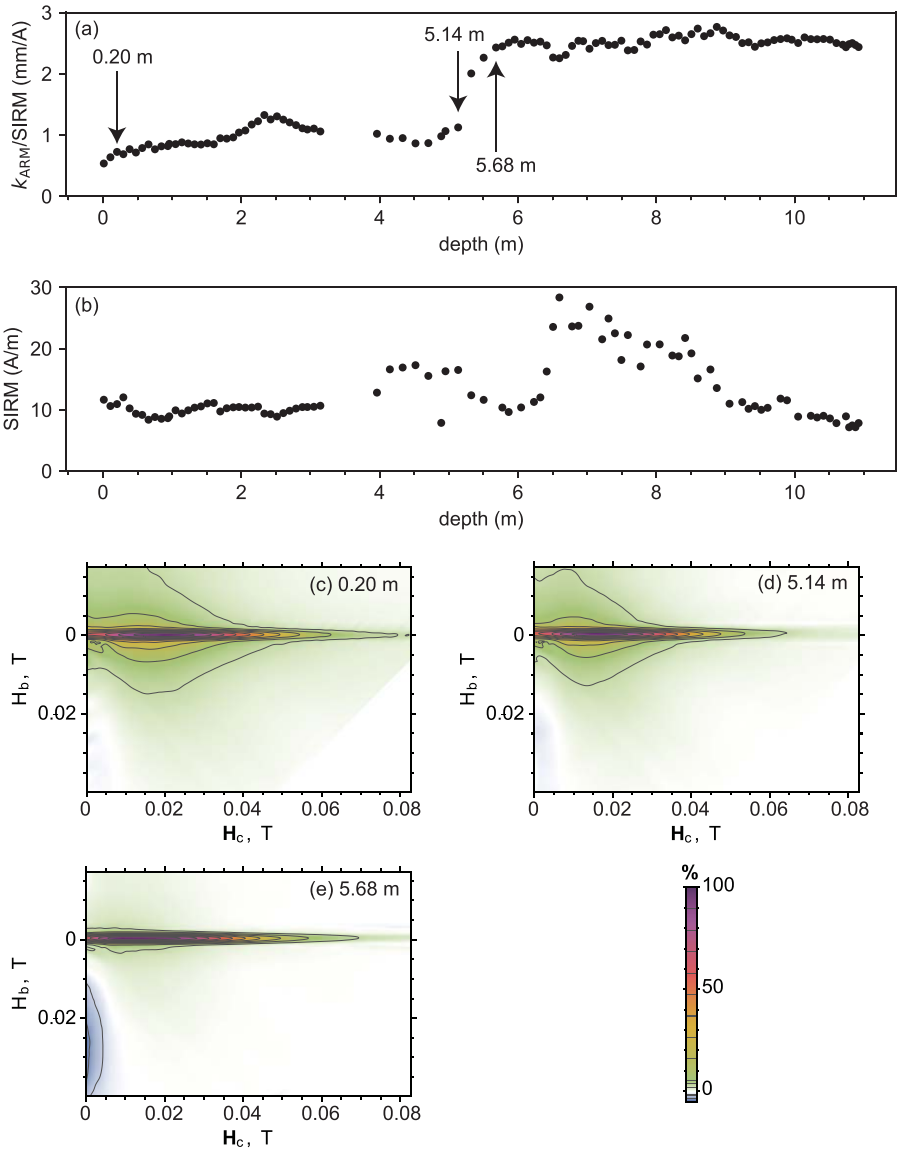

Figure 2. (a) Depth variation of *k*ARM/IRM. (b) Depth variation of SIRM. (c–e) Representative FORC diagrams; (c) 0.20 m, (d) 5.14 m, and (e) 5.68 m. FORC diagrams were calculated using the VARIFORC parameters; *S*0=8, λ=0.1, *Hb*0=0.0004, *sb*0=3, and *w*0 = 0.0005.

of two linear trends. The mixing of S ratios is linear in terms of the SIRM mixing ratio of magnetic phases when magnetostatic interaction is negligible, although it is nonlinear relative to mass mixing ratio (e.g., Heslop, 2009). Thus, the simplest interpretation of the trends is that there are three magnetic components. In particular, one of the trends shows near-saturation in $S_{-0.1}$. This is possible only when there are more than one magnetic component with distinct coercivity distributions which essentially saturate at 0.1 T.

We compare the contrasting coercivity spectra below 5.69 m and above 5.15 m as measured by the IRM acquisition gradient (Figure 4). Above 5.15 m, all curves show nonzero values above 0.1 T. The main variation is in the magnitude of the high field envelope of the curves. In contrast, below 5.69 m, the IRM gradient curves are narrowly peaked, and are close to zero above 0.1 T. The main variation is in the peak position and the magnitude of the low field envelope of the curves.

On the basis of the observations of the S ratios and the IRM gradients, we chose to use three endmembers to model the IRM acquisition curves. In fact, the coefficient of determination of the three-endmember model (0.994) is clearly higher than that of a two-endmember model (0.960), but it is not much lower than

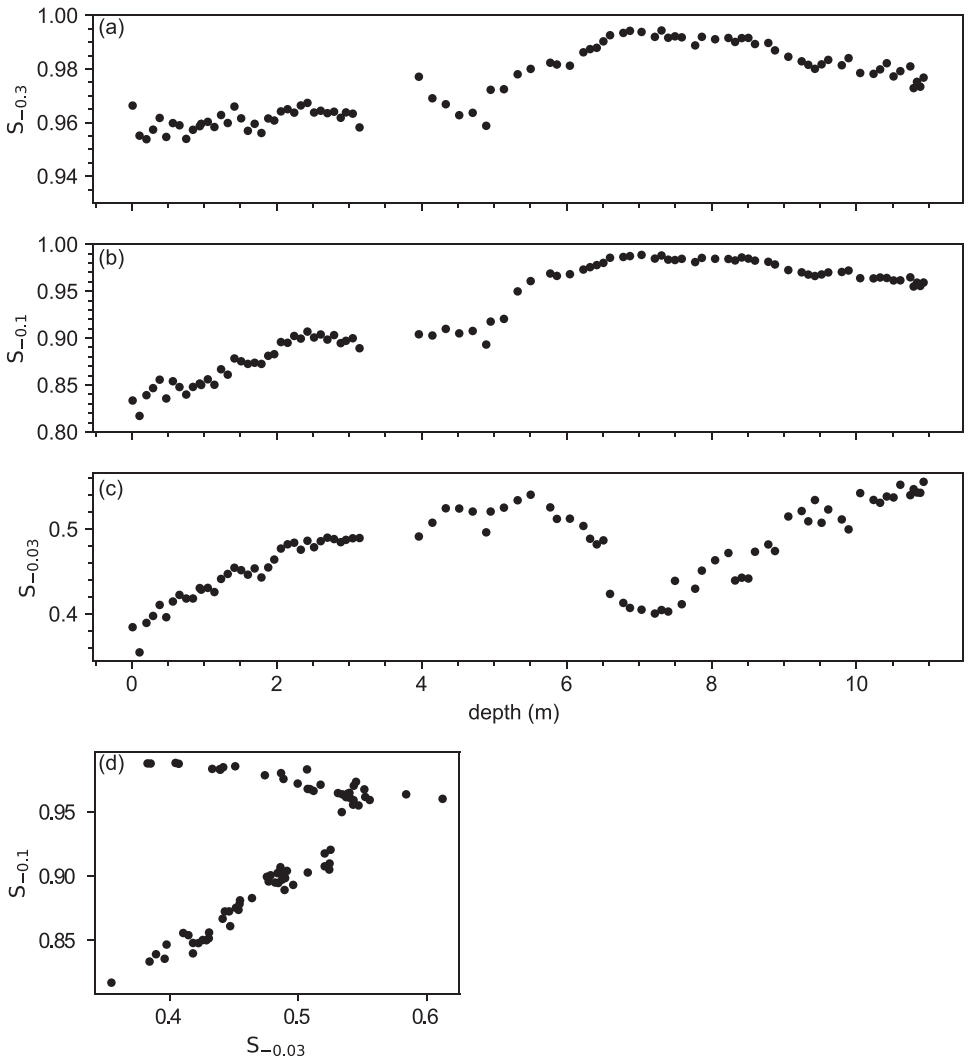

Figure 3. Results of S ratio measurements. (a) Depth variation of $S_{-0.3}$. (b) Depth variation of $S_{-0.1}$. (c) Depth variation of $S_{-0.03}$. (d) Cross plot of $S_{-0.1}$ versus $S_{-0.03}$.

that of a four-endmember model (0.998). Figure 5 shows the shapes and depth variations of these endmembers. As expected, we have two endmembers (EM1 and EM2) with narrow peak and IRM gradient close to zero above 0.1 T, and one endmember (EM3) with broader peak extending above 0.1 T. EM1 and EM2 dominate the magnetic signal of the sediments below 5.3 m where minimal magnetostatic interaction is inferred by the *k*ARM/IRM ratios and the FORC diagrams. We interpret that EM1 and EM2 represent magnetofossils. In contrast, the relative contribution of EM3 first rises sharply up-core from 5.69 to 5.15 m and then gradually toward the core top. This behavior matches that of terrigenous magnetic minerals inferred by the *k*ARM/IRM, the FORC diagrams, and $S_{-0.1}$. We therefore interpret that EM3 represents a terrigenous component. The IRM gradients of EM1 and EM2 are negatively skewed, a behavior expected for normal particle assemblages (Egli, 2003). EM3 is more symmetric with weak positive skewness, implying that the EM3 may be composed of multiple minerals such as maghemite, hematite, or goethite, as expected for a terrigenous component.

Parameters to characterize the IRM endmembers are listed in Table 1; μ, σ, q, and p were determined by fitting a skewed generalized Gaussian functions (Egli, 2003) to all endmembers on a logarithmic magnetic field scale (Figures 5a–5c).

The fit of EM3 is relatively poor, supporting the idea that this endmember may be composed of multiple minerals whose abundance vary in concert in the sediments. The remaining parameters were determined

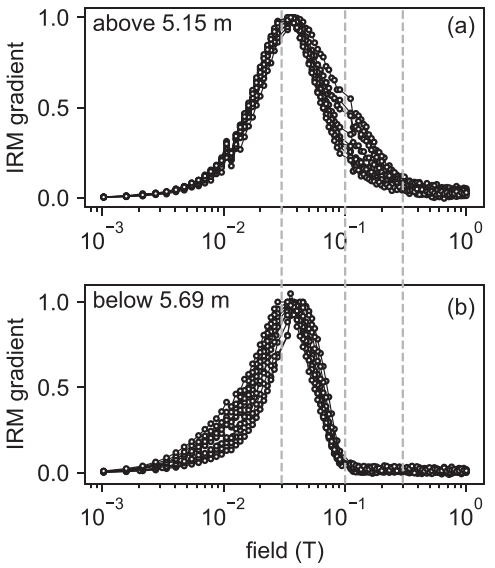

Figure 4. Normalized IRM gradients for (a) samples above 5.15 m and (b) samples below 5.69 m. Vertical gray dashed lines correspond to fields at 0.03, 0.1, and 0.3 T.

using cubic spline interpolation. The modal field is the magnetic field corresponding to the mode of IRM gradient, and the median field is the field at which 50% of the IRM at 0.3 T is acquired. We define S* ratios which are analogous to the S ratios, but calculated as the ratios to IRM at 0.3 T. Full saturation may not be achieved at 0.3 T, especially for EM3; therefore, the S* ratios would be slightly larger than the S ratios. The S* ratios of individual samples can be calculated from S ratios such that $S^*_{-0.03}=S_{-0.03}/S_{-0.3}$. The S* ratios of the endmembers bound the majority of the samples (Figure 6), indicating that the three endmembers explain the IRM acquisition behavior of the samples well. Some apparent misfit is probably due to the lack of intercalibration between the output field of the VSM and the pulse magnetizer.

The contributions of the two magnetofossil endmembers EM1 and EM2 vary systematically with depth (Figures 5f and 5g). Mostly the contribution of EM1 is larger; however, the contribution of EM2 has a prominent high at around 7.0 m. Above this depth, the absolute contribution of EM2 drops rather sharply from 6.8 to 6.4 m, while the relative contribution of EM2 decrease more gradually to ~5.3 m.

We also consider a simplified unmixing procedure using S* ratios. Egli (2004b) showed that when magnetic components occurring in samples are known, a mixture of N noninteracting magnetic components can be unmixed using the change in magnetization in N magnetic field intervals such as S ratios. In the sediment studied here, the endmember analysis indicates that there are three magnetic components. We will assume that all the samples contain the same components, and consider relative contributions instead of absolute contribution. Thus, we can use two S* ratios, $S^*_{-0.03}$ and $S^*_{-0.1}$, to estimate the relative contributions of EM1, EM2, and EM3 to IRM at 0.3 T, by considering the Figure 6 as a ternary plot. Formally, let c_i be the relative contribution of the ith endmember in a sample. Let $\mathbf{v_0}, \mathbf{v_1}, \mathbf{v_2}$ and $\mathbf{v_3}$ be vectors $(S^*_{-0.03}, S^*_{-0.1})$ of the sample, EM1, EM2, and EM3, respectively, and let $\mathbf{v_{1j}}$ be $(\mathbf{v_j}-\mathbf{v_1})$ where $j = 0$, 2, or 3. Then the relative contribution c_2 and c_3 are the solution to the equation:

$$\mathbf{v_{10}}=c_2\mathbf{v_{12}}+c_3\mathbf{v_{13}}, \tag{1}$$

and c_1 is simply

$$c_1=1-(c_2+c_3). \tag{2}$$

The absolute contributions of the endmembers can be calculated by multiplying the relative contributions by total IRM at 0.3 T, which in turn can be estimated from SIRM and $S_{-0.3}$. The resultant endmember contribution estimates are plotted in Figure 7.

Although the endmember contributions estimated from the S* ratios differ systematically from those derived from the IRM acquisition curves, their stratigraphic variation pattern matches very well. The systematic difference most likely reflects the difference in instruments used. We note that neither the VSM nor the pulse magnetizer has built-in methods to calibrate the absolute magnitude of output fields. Regardless, the analysis confirms that the peak in EM2 contribution at ~7 m is a singular event in the studied sediment.

4.3. Electron Microscopy

TEM observations revealed that magnetofossils, as identified by the size and shape, are abundant in the samples (Figure 8). The count of the two magnetofossil morphologies are listed in Table 2, and their depth variations are plotted in Figure 8c. The relative abundances of equant and bullet-shaped magnetofossils are consistent with the relative contributions of EM1 and EM2, respectively.

4.4. Organic Carbon Content

Figure 8d shows the depth variation of the TOC content. Overall, TOC content is low (¡0.12 wt %) throughout the sediments. Below 5.69 m, the TOC content is ~0.04 wt %, and no variation corresponding to the

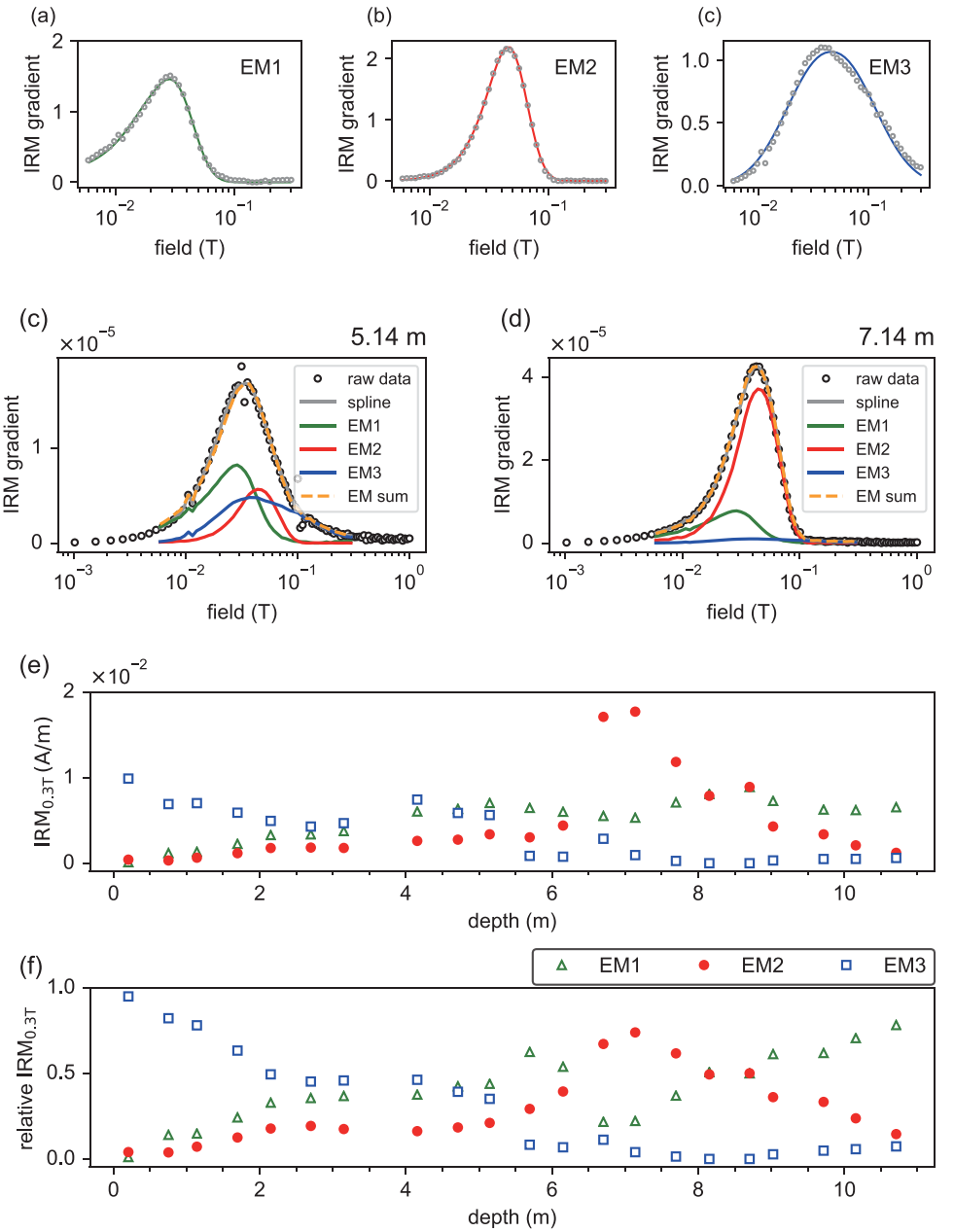

Figure 5. (a–c) The IRM gradient of endmembers EM1, EM2, and EM3. Lines are skewed generalized Gaussian fits. (d, e) Examples of endmember unmixing of IRM acquisitions. (d) Sample from 5.14 m. (e) Sample from 7.14 m. Circles represent raw measurement data, and the gray line is a spline interpolation of the data between 5 and 300 mT. Green, red, and blue lines represent EM1–3, respectively, and orange dashed line their sum. (f, g) Depth variation of (f) absolute and (g) relative endmember contributions to IRM at 0.3 T. Green open triangles represent EM1, the red solid circles EM2, and the blue open squared EM3.

increase in EM2 is observed. Above 5.15 m, the TOC content gradually increases up-core. This depth coincides with the appearance and increase of terrigeneous magnetic minerals quantified by EM3.

5. Discussion

5.1. The Magnetic Components and Their Carrier Minerals

On the basis of magnetic measurements and TEM observations, we showed that the red clay around Minamitorishima contains two magnetic components EM1 and EM2 corresponding to magnetofossils. The

Table 1
Characteristics of the IRM Acquisition Endmembers

Name	μ (T)	σ	q	p	Modal field (T)	Median field (T)	$S^*_{-0.03}$	$S^*_{-0.1}$
EM1	0.0214	0.475	0.400	2.44	0.0266	0.0213	0.715	0.991
EM2	0.0414	0.220	0.564	2.02	0.0404	0.0394	0.281	0.998
EM3	0.0460	0.385	1.00	2.17	0.0342	0.0434	0.326	0.826

Note. σ, q, p are expressed in the scale of $\log_{10}B$ where B is magnetic field in Tesla.

relative abundance of bullet-shaped magnetofossils correlates with the relative contribution of EM2, which is of higher coercivity than EM1. Previous studies of pelagic nannofossil ooze indicated that anisotropic magnetofossils have higher coercivity than isotropic ones (Yamazaki, 2012; Yamazaki & Ikehara, 2012). In lake sediments, Lascu and Plank (2013) also showed that biogenic magnetic components with distinct coercivities represent magnetofossils with different morphologies, with elongated magnetofossils being of higher coercivity than isotropic magnetofossils. This is also expected from theoretical calculations (Phatak et al., 2011). Although the chain length of magnetofossils can also affect magnetic coercivity (Muxworthy & Williams, 2009), the correlation between the direct TEM observation and the magnetic endmember contributions (Figure 8) shows that the most important factor controlling the relative contribution of EM1 and EM2 is the relative abundances of equant and bullet-shaped magnetofossils.

Two magnetofossil components have been reported from lake and marine sediments. They have mean IRM coercivities of ~40 and ~65 mT, and called BS and BH, respectively (e.g., Egli, 2004a; Yamazaki, 2012). The modal field of EM1 (26.6 mT) is clearly lower. In addition, the skewness of EM1 is larger than the magnetofossil assemblages analyzed by Egli (2004a). Using log-Gaussian decomposition technique of Kruiver et al. (2001), pelagic sediments from western North Pacific including red clay have been reported to contain a component with very low (~15 mT) coercivity with broad distribution (Yamazaki, 2008, 2009, 2012). A similar component was also reported in Egli (2004a) as EX component. Since the endmember analysis does not assume log-Gaussian functions, we suggest that EM1 also includes this signal. Egli (2004a) considered EX component may be ultrafine particles produced by iron-reducing bacteria. Because the red clay is in oxic condition, iron-reducing bacteria are unlikely to be widespread. Instead, we propose this signal may reflect oxic degradation of magnetofossils, such as maghemitization.

The modal field of EM2 (40.4 mT) is also lower than typical BH component. Although elongated, the aspect ratio of the bullet-shaped magnetofossils in the studied sediments (Figure 8a) appears to be lower than that reported from sediments other than red clay (e.g., Hesse, 1994; Roberts et al., 2013; Yamazaki, 2012; Yamazaki & Ikehara, 2012). We propose that the difference in morphology accounts for the difference in coercivity between EH2 and BH.

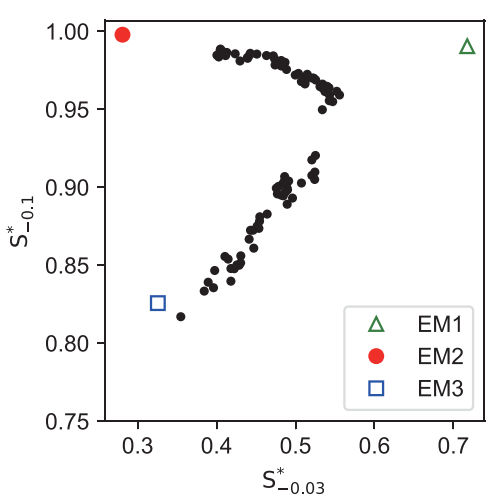

Figure 6. Cross plot of $S^*_{-0.1}$ versus $S^*_{-0.03}$. Black dots represent samples, green open triangle represents EM1, red solid circle represents EM2, and blue open square represents EM3.

5.2. Depth Variation of Magnetofossil Morphology

Bullet-shaped magnetofossil content quantified by EM2 has a prominent high at 7.0 m. Several studies indicated that anisotropic magnetofossils reflect less oxic conditions than isotropic magnetofossils (Egli, 2004a; Hesse, 1994; Yamazaki & Kawahata, 1998), although Lean and McCave (1998) reported the opposite trends from a contourite drift. On the other hand, in oligotrophic environments, magnetofossil abundance often increases under enhanced organic carbon flux (Roberts et al., 2011; Savian et al., 2014). In the studied sediments, the SIRM variation (Figure 2b) indicates that magnetofossil abundance is high at ~7 m. High organic carbon flux into the sediment, caused either by increased flux to the seafloor or enhanced preservation due to less-oxygenated deep water, would lead to shallower oxygen penetration in the sediments. Taken together, we propose that both the high proportion of bullet-shaped magnetofossils and the high abundance of magnetofossils at ~7 m were caused by a high organic carbon flux that resulted in less oxic conditions.

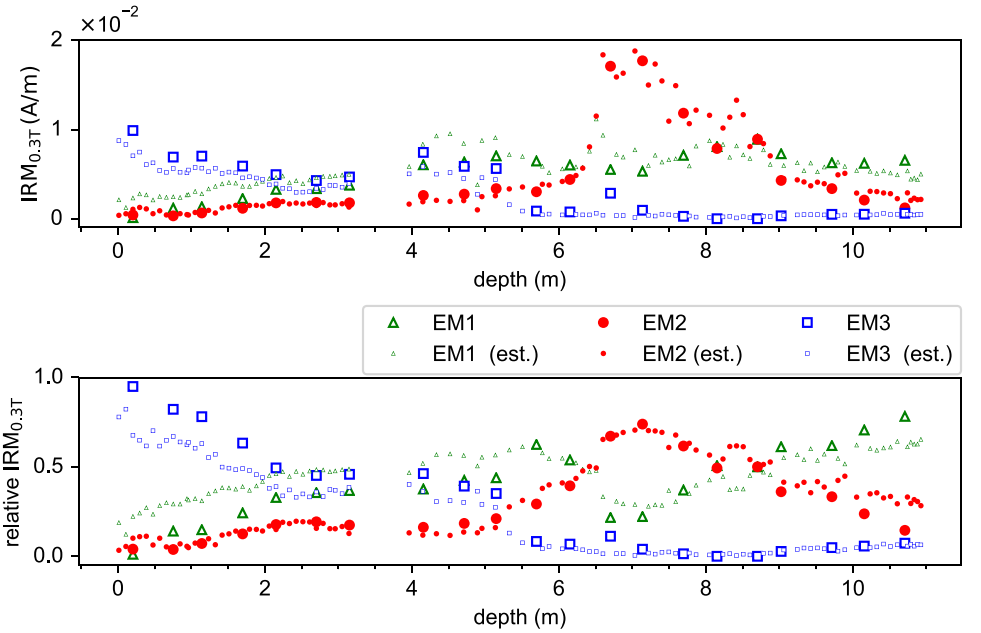

Figure 7. Endmember contributions estimated from the S* ratios. (a) Depth variation of absolute contribution to IRM at 0.3 T. (b) Depth variation of relative contribution to IRM at 0.3 T. Green open triangles represent EM1, red solid circles represent EM2, and blue open squares represent EM3. Larger symbols represent contributions directly derived by endmember modeling of IRM acquisitions.

The increase in the EM2 contribution is not reflected in the TOC content (Figure 8d). This is not surprising as oxic conditions promote remineralization of organic carbon (e.g., Canfield, 1994), so past organic carbon flux is not preserved as the TOC content. This result emphasizes the value of magnetofossils as paleoenvironmental tracers. On the other hand, the apparent positive correlation between EM3 and the TOC content draws attention. We speculate that the remaining organic carbon in the sediments may be largely terrigenous. Terrigenous organic compounds have been detected in open ocean aerosols (e.g., Peltzer & Gagosian, 1989) and sediments (Jia et al., 2012). In addition, terrigenous organic matter is considered to be more resistant to remineralization than marine organic matter (Burdige, 2005; Prahl et al., 1997). To our knowledge, the degradation of terrigenous organic matter in pelagic red clay has not been examined, but this is beyond the scope of the present study.

The absolute contribution of equant magnetofossils (EM1) remains almost unchanged while the contribution of bullet-shaped magnetofossils increases significantly to a maximum of ∼7 m (Figures 5 and 7). We consider two scenarios to explain this contrasting behavior. First, sedimentation rate may have been high in this interval, lowering the apparent abundance of equant magnetofossils. Although increased organic carbon flux could have accompanied increased deposition of biological shells, microfossils in these intervals are very rare, which is consistent with other intervals in the sediments. Therefore, we do not favor this possibility. Alternatively, the formation of equant magnetofossils may have been limited by other factors than organic carbon such as bioavailable iron (Roberts et al., 2011). Even with increased organic carbon flux, red clay is unlikely to achieve iron reducing conditions, and dissolved iron concentration should have been very low. Magnetotactic bacteria producing bullet-shaped magnetofossils may be better at utilizing organic carbon to uptake iron. This speculation needs to be tested by studying living magnetotactic bacteria in red clay.

5.3. Constraints on the Age and Location of the Magnetofossil Morphology Change

Although the age and paleoposition for the increased bullet-shaped magnetofossils in the sediments are unknown at present, rough constraints can be based on comparison with ocean drilling Sites. At the nearby Site 800, brown pelagic clay was underlain by brown chert, and the top of the chert was dated as late Campanian based on micropaleontology (Lancelot et al., 1990), and as ∼75 Ma based on agglutinated foraminifers (Wightman & Kuhnt, 1992). This gives the lower age bound of our red clay. On the other hand, many

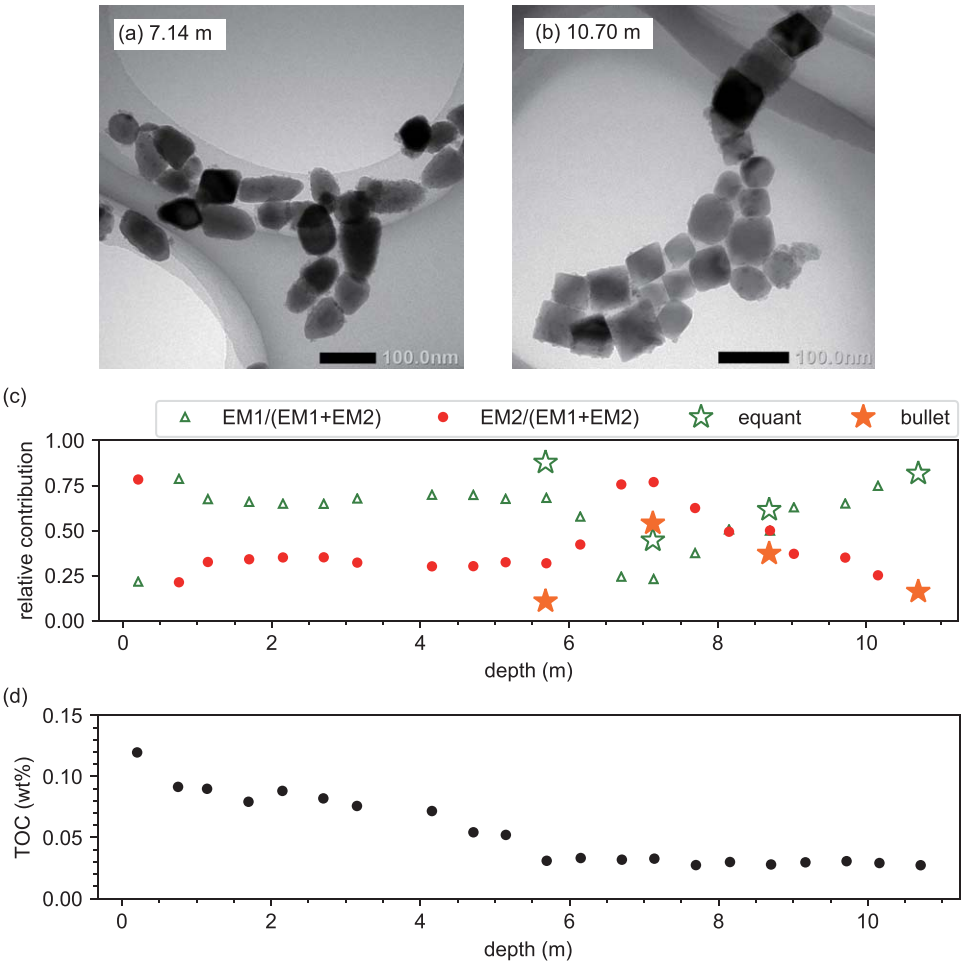

Figure 8. (a, b) TEM images of magnetic separates from (a) 7.14 m with abundant bullet-shaped magnetofossils, and (b) 10.70 m with abundant equant magnetofossils. (c) Depth variation of the relative abundance of equant and bullet-shaped magnetofossils, together with relative contribution of EM1 and EM2. Open green stars represent equant magnetofossils, solid red stars represent bullet-shaped magnetofossils, open green triangles represent EM1, and solid red circles represent EM2. (d) Depth variation of the total organic carbon (TOC) content.

western Pacific sites record increase of aeolian flux since ~25 Ma, possibly reflecting the progressive aridification of Asian interior (e.g., Zhang et al., 2016). It is tempting to correlate the up-core increase in the contribution of terrigenous magnetic endmember (EM3) with the increased aeolian flux. An obvious caveat is that we do not have the age-depth relationship, so we cannot convert the endmember contribution per volume into flux. Nonetheless, we argue that the overall trend can be used for correlation. In pelagic red clay, the aeolian component often accounts for more than 50 wt % of the bulk sediments (e.g., Janecek & Rea, 1983). Therefore, an increase in aeolian flux most likely results in increase in sedimentation rate. The variation in the EM3 contribution per volume neglects this change in sedimentation rate, so it is likely to be a conservative image of the variation in aeolian flux. Because the EM3 contribution is consistently low below ~5.3 m, we interpret that the sediments below ~5.3 m are older than ~25 Ma. While the possible existence of a hiatus makes it difficult to pinpoint the beginning of terrigenous contribution increase, the peak of bullet-shaped magnetofossil below ~6 m would be older than ~25 Ma. In summary, we tentatively estimate the age of the bullet-shaped magnetofossil increase to be between ~75 and ~25 Ma.

Between ~75 and ~25 Ma, Minamitorishima could have crossed the equator due to the Pacific plate motion, depending on the plate motion model assumed (e.g., Nakamura et al., 2016). Because the

Table 2
TEM Counts of Magnetofossil Morphologies

Depth (m)	Equant	Bullet-shaped	Elongated	Total
5.69	1059	130	18	1,207
7.14	614	744	20	1,378
8.69	833	167	17	1,354
10.70	846	167	23	1,036

increase in bullet-shaped magnetofossil abundance likely reflects higher organic carbon flux, one may speculate that this corresponds to the higher surface productivity near the equator. However, we feel this scenario is unlikely. On the basis of the nannofossil assemblage at Site 800, Erba (1992) identified migration into a high-fertility zone from the south in the middle Albian limestone that underlay the brown chert. This means that limestone and chert were deposited when this region was under the equatorial high productivity zone. Although it is still possible that part of the red clay was also deposited in the high productivity zone, the peak of bullet-shaped magnetofossil abundance shown here occurs in the middle of the red clay unit. The acoustic profile at the site KR13-02 PC05 (Nakamura et al., 2016) showed that the thickness of pelagic red clay is ~30 m. This indicates that ~20 m of red clay underlay the sediments studied here. Therefore, migration into the high productivity region cannot explain the start of the bullet-shaped magnetofossil increase in a simple way. If this interpretation is correct, the increase of the bullet-shaped magnetofossils in the sediments reflects some paleoceanographic events that caused an increase in organic carbon flux to the pelagic seafloor. Further research on the age and geographical distribution of the bullet-shaped magnetofossil occurrence in Pacific red clay is warranted to test this hypothesis.

6. Conclusions

Rock magnetic measurements and TEM observations showed that the pelagic red clay around Minamitorishima contains abundant magnetofossils. S ratios and IRM acquisition curve analysis revealed that the sediments contain three magnetic components: two components (EM1 and EM2) corresponding to magnetofossils, and one (EM3) corresponding to terrigenous magnetic minerals. Direct TEM observation indicates that EM1 represents the abundance of equant magnetofossils, while EM2 represents contribution of bullet-shaped magnetofossils.

Generally the EM1 contribution is higher than that of EM2; however, the EM2 contribution revealed an increase from the bottom of the sediments to ~7 m where it is higher than EM1, indicating. This indicates an increase in bullet-shaped magnetofossils. The increase of EM2 contribution corresponds to the increase in SIRM. These changes may be explained by increase in organic carbon flux to the sediments.

Lithostratigraphic correlation with nearby Site 800 indicates that the sediments studied here are younger than late Campanian. In addition, assuming that the variation in EM3 reflects the change in aeolian flux, we estimate that the increase in bullet-shaped magnetofossils is older than ~25 Ma. Age constraints, as well as the acoustic thickness of red clay (Nakamura et al., 2016), imply that the increase in bullet-shaped magnetofossils is not controlled by the plate motion into the equatorial high productivity zone. Rather, this magnetofossil morphology change is likely to reflect paleoceanographic events. The age and geographical distribution of this magnetofossil morphology change needs to be studied to link it to specific geological events.

For sediments dominated by magnetofossils, S ratios with back field lower than 0.1 T would be useful tools to unmix magnetic components. The contribution of endmembers defined from IRM acquisitions can be estimated with simple calculation using a few S ratios. Because the measurement of S ratios is much faster than that of IRM acquisition curves or FORCs, this provides a way to increase the spatial resolution of magnetic unmixing when lithology is relatively uniform. In addition, S ratios can be measured precisely using cryogenic magnetometers without pretreatment. To fully utilize S ratios in magnetic unmixing, better inter-instrumental and interlaboratory calibration will be essential.

Acknowledgments
The cruise MR15-E01 Leg2 was conducted as a part of Strategic Innovation Program (SIP), New-generation Technology for Ocean Resources Survey. Figure 1b was generated using multi-beam echo sounder data kindly provided by Dr. Shiki Machida.We thank Drs. David Heslop and Ramon Egli for help in the software usage. We thank Nobuhiro Ogawa for assistance with TEM observations, and Naomi Takahashi and Cao Cong for assistance with the TOC analysis. We also thank Dr. Kentaro Nakamura for discussion about stratigraphy of sediments around Minamitorishima. We deeply thank Prof. von Dobeneck and an anonymous reviewer for detailed and constructive reviews. Main data are available from supporting materials. All data are available in Zenodo data repository (https://doi.org/10.5281/zenodo.896990). This study was partly supported by JSPS KAKENHI Grant numbers JP17H01361, JP16K13896, and JP15H03740.

References

Bloemendal, J., Lamb, B., & King, J. (1988). Paleoenvironmental implications of rock-magnetic properties of late Quaternary sediment cores from the eastern Equatorial Atlantic. *Paleoceanography*, *3*(1), 61–87.

Burdige, D. J. (2005). Burial of terrestrial organic matter in marine sediments: A re-assessment. *Global Biogeochemical Cycles*, *19*(4), GB4011. https://doi.org/10.1029/2004GB002368

Canfield, D. E. (1994). Factors influencing organic carbon preservation in marine sediments. *Chemical Geology*, *114*(3), 315–329.

Cramer, B., Toggweiler, J., Wright, J., Katz, M., & Miller, K. (2009). Ocean overturning since the Late Cretaceous: Inferences from a new benthic foraminiferal isotope compilation. *Paleoceanography*, *24*(4), PA4216. https://doi.org/10.1029/2008PA001683

D'Hondt, S., Inagaki, F., Zarikian, C. A., Abrams, L. J., Dubois, N., Engelhardt, T., . . . Ziebis, W. (2015). Presence of oxygen and aerobic communities from sea floor to basement in deep-sea sediments. *Nature Geoscience*, *8*(4), 299–304.

D'Hondt, S., Spivack, A. J., Pockalny, R., Ferdelman, T. G., Fischer, J. P., Kallmeyer, J., . . . Stancin, A. M. (2009). Subseafloor sedimentary life in the South Pacific Gyre. *Proceedings of the National Academy of Sciences*, *106*(28), 11,651–11,656.

Dinarès-Turell, J., Hoogakker, B. A., Roberts, A. P., Rohling, E. J., & Sagnotti, L. (2003). Quaternary climatic control of biogenic magnetite production and eolian dust input in cores from the Mediterranean Sea. *Palaeogeography, Palaeoclimatology, Palaeoecology*, *190*, 195–209.

Egli, R. (2003). Analysis of the field dependence of remanent magnetization curves. *Journal of Geophysical Research*, *108*, 2081. https://doi.org/10.1029/2002JB002023

Egli, R. (2004a). Characterization of individual rock magnetic components by analysis of remanence curves, 1. unmixing natural sediments. *Studia Geophysica et Geodaetica*, *48*(2), 391–446.

Egli, R. (2004b). Characterization of individual rock magnetic components by analysis of remanence curves. 3. bacterial magnetite and natural processes in lakes. *Physics and Chemistry of the Earth*, *29*(13), 869–884.

Egli, R., Chen, A. P., Winklhofer, M., Kodama, K. P., & Horng, C.-S. (2010). Detection of noninteracting single domain particles using first-order reversal curve diagrams. *Geochemistry, Geophysics, Geosystems*, *11*, Q01Z11. https://doi.org/10.1029/2009GC002916

Erba, E. (1992). Middle cretaceous calcareous nannofossils from the western Pacific (leg 129): Evidence for paleoequatorial crossings. In *Proceedings of the Ocean Drilling Program, Scientific Results* (vol. 129, pp. 189–201). College Station, TX: Ocean Drilling Program. https://doi.org/10.2973/odp. proc.sr.129.119.1992

Farina, M., Kachar, B., Lins, U., Broderick, R., & Lins de Barros, H. (1994). The observation of large magnetite (Fe_3O_4) crystals from magnetotactic bacteria by electron and atomic force microscopy. *Journal of Microscopy*, *173*(1), 1–8.

Fischer, J. P., Ferdelman, T. G., D'hondt, S., Røy, H., & Wenzhöfer, F. (2009). Oxygen penetration deep into the sediment of the South Pacific gyre. *Biogeosciences*, *6*(8), 1467–1478.

Heslop, D. (2009). On the statistical analysis of the rock magnetic S-ratio. *Geophysical Journal International*, *178*(1), 159–161.

Heslop, D., & Dillon, M. (2007). Unmixing magnetic remanence curves without a priori knowledge. *Geophysical Journal International*, *170*(2), 556–566.

Heslop, D., Roberts, A. P., & Chang, L. (2014). Characterizing magnetofossils from first-order reversal curve (FORC) central ridge signatures. *Geochemistry, Geophysics, Geosystems*, *15*, 2170–2179. https://doi.org/10.1002/2014GC005291

Hesse, P. P. (1994). Evidence for bacterial palaeoecological origin of mineral magnetic cycles in oxic and sub-oxic Tasman sea sediments. *Marine Geology*, *117*(1–4), 1–17.

Iijima, K., Yasukawa, K., Fujinaga, K., Nakamura, K., Machida, S., Takaya, Y., . . . Kato, Y. (2016). Discovery of extremely REY-rich mud in the western North Pacific Ocean. *Geochemical Journal*, *50*, 557–573.

Janecek, T. R., & Rea, D. K. (1983). Eolian deposition in the northeast Pacific Ocean: Cenozoic history of atmospheric circulation. *Geological Society of America Bulletin*, *94*(6), 730–738.

Jia, G., Li, Z., Peng, P., & Zhou, L. (2012). Aeolian n-alkane isotopic evidence from North Pacific for a Late Miocene decline of C_4 plant in the arid Asian interior. *Earth and Planetary Science Letters*, *321*, 32–40.

Kirschvink, J. L., & Chang, S.-B. R. (1984). Ultrafine-grained magnetite in deep-sea sediments: Possible bacterial magnetofossils. *Geology*, *12*(9), 559–562.

Kirschvink, J. L., Kobayashi-Kirschvink, A., & Woodford, B. J. (1992). Magnetite biomineralization in the human brain. *Proceedings of the National Academy of Sciences*, *89*(16), 7683–7687.

Kobayashi, A., Kirschvink, J. L., Nash, C. Z., Kopp, R. E., Sauer, D. A., Bertani, L. E., . . . Taguchi, T. (2006). Experimental observation of magnetosome chain collapse in magnetotactic bacteria: sedimentological, paleomagnetic, and evolutionary implications. *Earth and Planetary Science Letters*, *245*(3), 538–550.

Kopp, R. E., & Kirschvink, J. L. (2008). The identification and biogeochemical interpretation of fossil magnetotactic bacteria. *Earth-Science Reviews*, *86*(1), 42–61.

Kopp, R. E., Raub, T. D., Schumann, D., Vali, H., Smirnov, A. V., & Kirschvink, J. L. (2007). Magnetofossil spike during the paleocene-eocene thermal maximum: Ferromagnetic resonance, rock magnetic, and electron microscopy evidence from Ancora, New Jersey, United States. *Paleoceanography*, *22*(4), PA4103. https://doi.org/10.1029/2007PA001473

Kopp, R. E., Weiss, B. P., Maloof, A. C., Vali, H., Nash, C. Z., & Kirschvink, J. L. (2006). Chains, clumps, and strings: Magnetofossil taphonomy with ferromagnetic resonance spectroscopy. *Earth and Planetary Science Letters*, *247*(1), 10–25.

Kruiver, P. P., Dekkers, M. J., & Heslop, D. (2001). Quantification of magnetic coercivity components by the analysis of acquisition curves of isothermal remanent magnetisation. *Earth and Planetary Science Letters*, *189*(3), 269–276.

Lancelot, Y., Larson, R. *et al*. (1990). Site 800. In *Proceedings of the Ocean Drilling Program, Initial Reports* (Vol. 129, pp. 33–89). College Station, TX: Ocean Drilling Program. https://doi.org/10.2973/odp. proc.ir.129.102.1990

Lascu, I., & Plank, C. (2013). A new dimension to sediment magnetism: Charting the spatial variability of magnetic properties across lake basins. *Global and Planetary Change*, *110*, 340–349.

Lean, C., & McCave, I. (1998). Glacial to interglacial mineral magnetic and palaeoceanographic changes at Chatham Rise, SW Pacific Ocean. *Earth and Planetary Science Letters*, *163*(1), 247–260.

Lefèvre, C. T., Abreu, F., Schmidt, M. L., Lins, U., Frankel, R. B., Hedlund, B. P., & Bazylinski, D. A. (2010). Moderately thermophilic magnetotactic bacteria from hot springs in Nevada. *Applied and Environmental Microbiology*, *76*(11), 3740–3743.

Lefèvre, C. T., Frankel, R. B., Pósfai, M., Prozorov, T., & Bazylinski, D. A. (2011). Isolation of obligately alkaliphilic magnetotactic bacteria from extremely alkaline environments. *Environmental Microbiology*, *13*(8), 2342–2350.

Li, J., Wu, W., Liu, Q., & Pan, Y. (2012). Magnetic anisotropy, magnetostatic interactions and identification of magnetofossils. *Geochemistry, Geophysics, Geosystems*, *13*, Q10Z51. https://doi.org/0.1029/2012GC004384

Lin, W., Bazylinski, D. A., Xiao, T., Wu, L.-F., & Pan, Y. (2014). Life with compass: diversity and biogeography of magnetotactic bacteria. *Environmental Microbiology*, *16*(9), 2646–2658.

Mewes, K., Mogollón, J. M., Picard, A., Rühlemann, C., Kuhn, T., Nöthen, K., & Kasten, S. (2014). Impact of depositional and biogeochemical processes on small scale variations in nodule abundance in the Clarion-Clipperton Fracture Zone. *Deep Sea Research Part I: Oceanographic Research Papers*, *91*, 125–141.

Mogollón, J. M., Mewes, K., & Kasten, S. (2016). Quantifying manganese and nitrogen cycle coupling in manganese-rich, organic carbon-starved marine sediments: Examples from the Clarion-Clipperton fracture zone. *Geophysical Research Letters*, *43*, 7114–7123. https://doi.org/10.1002/2016GL069117

Moskowitz, B. M., Frankel, R. B., & Bazylinski, D. A. (1993). Rock magnetic criteria for the detection of biogenic magnetite. *Earth and Planetary Science Letters*, *120*(3–4), 283–300.

Muxworthy, A. R., & Williams, W. (2009). Critical superparamagnetic/single-domain grain sizes in interacting magnetite particles: Implications for magnetosome crystals. *Journal of the Royal Society Interface*, *6*, 1207–1212. https://doi.org/10.1098/rsif.2008.0462

Nakamura, K., Machida, S., Okino, K., Masaki, Y., Iijima, K., Suzuki, K., & Kato, Y. (2016). Acoustic characterization of pelagic sediments using sub-bottom profiler data: Implications for the distribution of REY-rich mud in the Minamitorishima EEZ, western Pacific. *Geochemical Journal*, *50*(6), 605–619.

Norris, R., Turner, S. K., Hull, P., & Ridgwell, A. (2013). Marine ecosystem responses to Cenozoic global change. *Science*, *341*(6145), 492–498.

Nozaki, T. (2015). R/V MIRAI cruise report MR15-E01 Leg 2, strategic innovation program (SIP), new-generation technology for ocean resources survey (ZIPANG in ocean), "deep-sea mud sampling around the Minamitorishima offshore". Retrieved from http://www.godac.jamstec.go.jp/catalog/doc_catalog/metadataDisp/MR15-E01_leg2_all?lang=en.

Peltzer, E., & Gagosian, R. (1989). Organic geochemistry of aerosols over the Pacific Ocean. In R. A. Duce, J. P. Riley, R. Chester (Eds.), *Chemical Oceanography* (Vol. 10, pp. 281–338). London: Academic Press.

Petermann, H., & Bleil, U. (1986). Detection of live magnetotactic bacteria in South Atlantic deep-sea sediments. *Earth and Planetary Science Letters*, *117*(1–2), 223–228.

Petersen, N., von Dobeneck, T., & Vali, H. (1993). Fossil bacterial magnetite in deep-sea sediments from the South Atlantic Ocean. *Nature*, *320*(6063), 611–615.

Phatak, C., Pokharel, R., Beleggia, M., & De Graef, M. (2011). On the magnetostatics of chains of magnetic nanoparticles. *Journal of Magnetism and Magnetic Materials*, *323*(22), 2912–2922.

Pike, C. R., Roberts, A. P., & Verosub, K. L. (1999). Characterizing interactions in fine magnetic particle systems using first order reversal curves. *Journal of Applied Physics*, *85*(9), 6660–6667.

Prahl, F. G., De Lange, G. J., Scholten, S., & Cowie, G. L. (1997). A case of post-depositional aerobic degradation of terrestrial organic matter in turbidite deposits from the Madeira Abyssal Plain. *Organic Geochemistry*, *27*(3–4), 141–152.

Rea, D. K. (1994). The paleoclimatic record provided by Eolian deposition in the deep sea: The geologic history of wind. *Reviews of Geophysics*, *32*(2), 159–195.

Roberts, A. P., Florindo, F., Chang, L., Heslop, D., Jovane, L., & Larrasoaña, J. C. (2013). Magnetic properties of pelagic marine carbonates. *Earth-Science Reviews*, *127*, 111–139.

Roberts, A. P., Florindo, F., Villa, G., Chang, L., Jovane, L., Bohaty, S. M., . . . Gerald, J. D. F. (2011). Magnetotactic bacterial abundance in pelagic marine environments is limited by organic carbon flux and availability of dissolved iron. *Earth and Planetary Science Letters*, *310*(3), 441–452.

Roberts, A. P., Heslop, D., Zhao, X., & Pike, C. R. (2014). Understanding fine magnetic particle systems through use of first-order reversal curve diagrams. *Reviews of Geophysics*, *52*(4), 557–602.

Robertson, D., & France, D. (1994). Discrimination of remanence-carrying minerals in mixtures, using isothermal remanent magnetisation acquisition curves. *Physics of the Earth and Planetary Interiors*, *82*(3–4), 223–234.

Røy, H., Kallmeyer, J., Adhikari, R. R., Pockalny, R., Jørgensen, B. B., & D'hondt, S. (2012). Aerobic microbial respiration in 86-million-year-old deep-sea red clay. *Science*, *336*(6083), 922–925.

Savian, J. F., Jovane, L., Frontalini, F., Trindade, R. I., Coccioni, R., Bohaty, S. M., . . . Iacoviello, F. (2014). Enhanced primary productivity and magnetotactic bacterial production in response to middle Eocene warming in the Neo-Tethys Ocean. *Palaeogeography, Palaeoclimatology, Palaeoecology*, *414*, 32–45.

Shimono, T., & Yamazaki, T. (2016). Environmental rock-magnetism of Cenozoic red clay in the South Pacific Gyre. *Geochemistry, Geophysics, Geosystems*, *17*, 1296–1311. https://doi.org/10.1002/2015GC006062

Stolz, J. F., Chang, S.-B. R., & Kirschvink, J. L. (1986). Magnetotactic bacteria and single-domain magnetite in hemipelagic sediments. *Nature*, *321*(6073), 849–851.

Thompson, R., & Oldfield, F. (1986). *Environmental magnetism*. London, UK: Allen and Unwin.

Vali, H., von Dobeneck, T., Amarantidis, G., Förster, O., Morteani, G., Bachmann, L., & Petersen, N. (1989). Biogenic and lithogenic magnetic minerals in Atlantic and Pacific Deep Sea sediments and their paleomagnetic significance. *Geologische Rundschau*, *78*(3), 753–764.

von Dobeneck, T., Petersen, N., & Vali, H. (1987). Bakterielle magnetofossilien. *Geowissenschaften in Unserer Zeit*, *1*, 27–35.

Wightman, W. G., & Kuhnt, W. (1992). Biostratigraphy and paleoecology of late cretaceous abyssal agglutinated foraminifers from the western Pacific Ocean (deep sea drilling project hole 196a and 198a and ocean drilling program holes 800a and 801a). In *Proceedings of the Ocean Drilling Program, Scientific Results* (vol. 129, pp. 247–264). College Station, TX: Ocean Drilling Program. https://doi.org/10.2973/odp.proc.sr.129.148.1992

Yamazaki, T. (2008). Magnetostatic interactions in deep-sea sediments inferred from first-order reversal curve diagrams: Implications for relative paleointensity normalization. *Geochemistry, Geophysics, Geosystems*, *9*, Q02005. https://doi.org/10.1029/2007GC001797

Yamazaki, T. (2009). Environmental magnetism of Pleistocene sediments in the North Pacific and Ontong-Java Plateau: Temporal variations of detrital and biogenic components. *Geochemistry, Geophysics, Geosystems*, *10*, Q07Z04. https://doi.org/10.1029/2009GC002413

Yamazaki, T. (2012). Paleoposition of the Intertropical Convergence Zone in the eastern Pacific inferred from glacial-interglacial changes in terrigenous and biogenic magnetic mineral fractions. *Geology*, *40*(2), 151–154.

Yamazaki, T., & Ikehara, M. (2012). Origin of magnetic mineral concentration variation in the Southern Ocean. *Paleoceanography*, *27*(2), PA2206. https://doi.org/10.1029/2011PA002271

Yamazaki, T., & Ioka, N. (1997). Environmental rock-magnetism of pelagic clay: Implications for Asian Eolian input to the North Pacific since the Pliocene. *Paleoceanography*, *12*(1), 111–124.

Yamazaki, T., & Kawahata, H. (1998). Organic carbon flux controls the morphology of magnetofossils in marine sediments. *Geology*, *26*(12), 1064–1066.

Yamazaki, T., & Shimono, T. (2013). Abundant bacterial magnetite occurrence in oxic red clay. *Geology*, *41*(11), 1191–1194.

Zhang, W., Chen, J., Ji, J., & Li, G. (2016). Evolving flux of Asian dust in the North Pacific Ocean since the late Oligocene. *Aeolian Research*, *23*, 11–20.

Ziebis, W., McManus, J., Ferdelman, T., Schmidt-Schierhorn, F., Bach, W., Muratli, J., . . . Villinger, H. (2012). Interstitial fluid chemistry of sediments underlying the North Atlantic gyre and the influence of subsurface fluid flow. *Earth and Planetary Science Letters*, *323*, 79–91.